Chemical Engineering Science 320 (2026) 122273

Contents lists available at ScienceDirect

Chemical Engineering Science

journal homepage: www.elsevier.com/locate/ces

Wet particle collisions simulated using the local front reconstruction method, a DNS approach

A.H. Huijgen [a], T.J.A. Janssen [b], F. Bunke [c], S. Pietsch-Braune [c], S. Heinrich [c], J.A.M. Kuipers [b], M.W. Baltussen [a,*]

[a] Department of Chemical Engineering and Chemistry, Multiphase Flows for Energy Applications, Eindhoven University of Technology, P.O. Box 513, 5600 MB, Eindhoven, the Netherlands
[b] Department of Chemical Engineering and Chemistry, Multiphase Reactors Group, Eindhoven University of Technology, P.O. Box 513, 5600 MB, Eindhoven, the Netherlands
[c] Institute of Solids Process Engineering and Particle Technology, Hamburg University of Technology, Denickestraße 15, Hamburg, 21073, Germany

ARTICLE INFO

Keywords:
Wet collisions
Liquid injection
Liquid bridge
Direct numerical simulations
Immersed boundary method
Local front reconstruction method

ABSTRACT

In addition to particles and gas, liquid is sometimes introduced into fluidized beds to, for example, cool the reactor or to provide reactants. However, the introduction of liquids can lead to agglomeration, which may be desirable or undesirable. To control the formation and impact of these agglomerates on the process, it is important to understand the collision of wet particles. To effectively understand the collision dynamics of wet particles, this work investigates the interaction between a wet particle and a dry particle using a novel Front-Tracking (FT) approach in combination with an Immersed Boundary Method (IBM). After thorough verification, extensive simulations were conducted producing excellent agreement with the experimental results of Bunke et al. (Chemical Engineering Journal, 2024, vol. 489, 151016). From the simulation results, the primary source of energy dissipation was found to be the extension of the liquid bridge directly after the collision, where the liquid is transferred to the liquid bridge effectively causing the deceleration of the particle. The friction coefficient, which is affected by the lubrication by the liquid, is a material property that should be modeled using the experimental value. Based on the simulation results, effective collision parameters for the hard-sphere model are obtained.

1. Introduction

Fluidized beds are widely used in industries because of their excellent mass and heat transfer characteristics and particle mobility. In these systems, solid particles are suspended and fluidized by an upward gas flow, creating vigorous motion that improves contact between particles and fluids. When liquid is introduced into the bed, the particles might form agglomerates. These agglomerates can have different roles in the fluidized bed process. If the introduced liquid is a binder, the agglomerates will form raspberry-like porous particles. These newly formed particles have improved wettability and solubility, as a result of their controlled porosity. In some processes, the liquid is introduced as a reactant or is (one of) the product(s) whereas the particles act as a catalyst. The formed agglomerates reduce the efficiency of heat and mass transfer, which can cause operational problems such as channeling or defluidization (Milacic et al., 2023). For all of these applications, it is critical to understand how wet agglomerates form, grow, and disintegrate. A crucial step in the formation of agglomerates is the collision of the wet particles. If the entire kinetic energy dissipates during a collision, the particles aggregate. The formed complex is stabilized by the capillary forces and requires additional force to disintegrate. These aggregates will grow and form agglomerates.

To unravel the complex dynamics of agglomerate formation, it is crucial to understand the wet particle collisions, for which there are generally two approaches. In the first approach, particle collisions are investigated experimentally. As experiments are costly and time-consuming, and it is challenging to measure and mimic physical phenomena in a lab-scale setup, only limited research has been done in this direction. In addition there are limitations regarding the permissible size of the impacting particles due to the difficulties to observe (especially) the evolution of rotational motion.

Donahue and co-workers have used a wet Newton's Cradle to investigate the lower restitution coefficient if a viscous liquid is added (Donahue et al., 2010a,b, 2012). Another relevant experiment is the collision of a particle with a thin liquid sheet. In the rebound phase, a liquid bridge is formed, similar to wet particle collisions. This is widely

* Corresponding author.
E-mail address: m.w.baltussen@tue.nl (M.W. Baltussen).

https://doi.org/10.1016/j.ces.2025.122273
Received 30 June 2025; Accepted 22 July 2025
Available online 5 August 2025

Table 1
Overview of interface techniques with their advantages and disadvantages. (Adapted from Van Sint Annaland et al. (2005)).

Method	Advantage	Disadvantage
Front-Tracking	Extremely accurate Robust Controlled merging and breakage	Mapping interface mesh onto Eulerian mesh Dynamic remeshing required Sub-grid model required for topological changes
Level set	Conceptually simple Easy to implement	Limited accuracy Mass conservation
VOF	Relatively simple Accurate	Difficult to implement in 3D Automatic merging and breakage
Marker and Cell	Extremely accurate Robust	Computationally expensive Re-distribution of markers required

done experimentally and numerically in the literature (Jain et al., 2012; Tang et al., 2017; Antonyuk et al., 2009; Ma et al., 2016; Shao et al., 2022). The collision of freely moving wet particles adds additional challenges in measuring and controlling the wetting of both particles. Until now, only Bunke and co-workers have managed to perform wet particle collisions. In their work, a wetted particle collided with a dry particle while tracking their positions in three dimensions (Bunke et al., 2024). We will use the work of Bunke et al. (2024) as a validation of the simulations in this work.

Another approach to study the dynamics of wet particle collisions is to use numerical simulations. Accurate numerical simulations of multiphase systems rely on an accurate description of the gas-liquid interface. Several different techniques for describing the gas-liquid interface are shown in Table 1. The most promising techniques for the simulation of agglomerates are the Front-Tracking and the Volume of Fluid (VOF) method, because of the accuracy and volume conservativeness, respectively. In VOF, the position of the interface is indicated by a color function. Kan and co-workers have used VOF to simulate the collision of partially wetted particles. In their work, the particles are represented by a Constrained Interpolation Profile (CIP) method in combination with an Immersed Boundary Method to represent the particles (Kan et al., 2015, 2016, 2018). In the work of Shao et al., the Volume of Fluid method is used in combination with overset grid method from Ansys Fluent to simulate the collision of a dry particle with a partially wet stationary particle (Shao et al., 2022). In their further efforts, they used this technique to conduct an exploratory study of the collision of a fully wet particle with a dry particle (Fan et al., 2024). Despite these advances, a comprehensive understanding of wet particle collisions, especially in scenarios involving freely moving particles, remains challenging because of experimental and computational challenges.

This study aims to address these gaps by simulating the collision of a wet and dry particle using a validated, state-of-the-art Front-Tracking approach, the Local Front Reconstruction Method (LFRM). LFRM represents the interface as a triangulated mesh, like the original Front-Tracking method, but enables the detection and handling of major topological changes (i.e. break-up and coalescence). Hereby, giving it similar capabilities as VOF, LFRM has been shown to offer improved accuracy over VOF at similar grid resolutions for droplet-droplet collisions (Huijgen et al., 2024a,b).

2. Numerical method

In this study, Direct Numerical Simulations are employed to simulate this three-phase system. The fluids are assumed to be Newtonian, immiscible, incompressible, and isothermal. The solid is assumed to be non-porous with a no-slip boundary at the surface. By applying the one-fluid formulation, the velocity and pressure fields are calculated from the continuity and Navier-Stokes equations in Eqs. (1) and (2).

$$\nabla \cdot \boldsymbol{u} = 0 \tag{1}$$

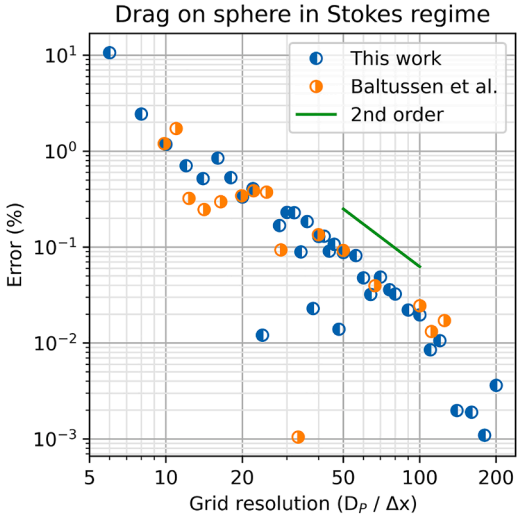

Fig. 1. Calculated drag force compared to the analytical value for flow around a sphere in stokes flow, compared to literature (Baltussen, 2015).

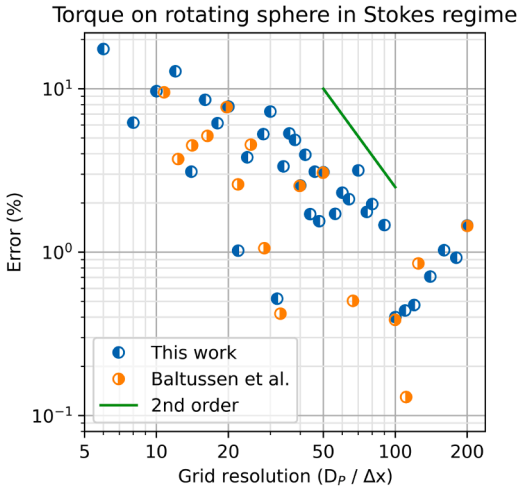

Fig. 2. Calculated drag force compared to the analytical value for flow around a sphere in stokes flow, compared to literature (Baltussen, 2015).

$$\rho\frac{\partial \boldsymbol{u}}{\partial t} = -\nabla p - \rho\nabla\cdot(\boldsymbol{uu}) - \nabla\cdot\boldsymbol{\tau} + \rho\boldsymbol{g} + \boldsymbol{F_\sigma} \tag{2}$$

Where the fluid stress tensor is defined as $\boldsymbol{\tau} = -\mu[\nabla\boldsymbol{u} + (\nabla\boldsymbol{u})^T]$, $\boldsymbol{u}$ is the velocity, p the pressure, $\boldsymbol{g}$ the gravitational constant, and $\boldsymbol{F_\sigma}$ a body force representing the surface tension (further explained in Section 2.1). The density (ρ) and the viscosity (μ) are obtained by linear averaging and harmonic averaging of these properties in the liquid phase ($\phi = 1$) and

the gas phase ($\phi = 0$), according to Eqs. (3) and (4). The color function ϕ indicates the fractional liquid occupation, which is explained further in Section 2.1.

$$\rho = \rho_l \phi + \rho_g (1 - \phi) \tag{3}$$

$$\frac{\rho}{\mu} = \frac{\rho_l}{\mu_l}\phi + \frac{\rho_g}{\mu_g}(1 - \phi) \tag{4}$$

This highly coupled system of equations is solved using a two-step projection-correction method. The first step consists of a predictor step to compute the velocity based on Eq. (2). The second-order Barton scheme is used to discretize the convective term, and the diffusive term is discretized using a second-order central difference scheme (Van Sint Annaland et al., 2005; Van Leer, 1977; Centrella and Wilson, 1984). This equation is solved explicitly except for the viscous stress term, which is solved semi-implicitly according to the formulation of Dijkhuizen et al. (2010). The decoupled set of linear equations is solved using the Biconjugate gradient stabilized method (BiCGSTAB2) (van der Vorst, 1992), using the incomplete LU-decomposition preconditioner from the Ifpack2 package of the Trilinos project (Team The Trilinos Project, 2023). To satisfy the continuity equation (Eq. (1)), the velocity prediction is corrected using the correction factor $\delta p = p^{n+1} - p^n$, in Eqs. (5) and (6).

$$\nabla \cdot \left[\frac{\Delta t}{\rho^n}\nabla(\delta p)\right] = \nabla \cdot \boldsymbol{u}^* \tag{5}$$

$$\boldsymbol{u}^{n+1} = \boldsymbol{u}^* - \frac{\Delta t}{\rho^n}\nabla \delta p \tag{6}$$

With $\boldsymbol{u}^*$ being the predicted velocity from the first step. p^n and p^{n+1} are the pressures at the previous and current time step, respectively. The time step is adjusted during the simulation to satisfy both the Courant-Friedrichs-Lewy (CFL) condition and the capillary time step constraint, as shown in Eq. (7) (Brackbill et al., 1992; Mirsandi et al., 2018).

$$\Delta t < \min\left(\Delta t_{CFL}, \Delta t_{Capillary}\right) = \min\left(\frac{\Delta}{v_{\max}}, \sqrt{\frac{(\rho_l + \rho_g)\Delta^3}{4\pi\sigma}}\right) \tag{7}$$

with Δ being the grid size, $v_{\max}$ the maximum velocity in the entire computational domain and σ the surface tension.

2.1. Gas-liquid interface

The representation of the gas-liquid interface is key in accurately describing the dynamics of the encounter process. For binary droplet collisions, the Local Front Reconstruction Method (LFRM) showed improved performance compared to the Volume of Fluid (VOF) method at similar grid resolutions (Huijgen et al., 2024a,b). Therefore, this work will also use LFRM to represent the gas-liquid interface. In LFRM, this interface is explicitly tracked by a triangular mesh, which allows topological changes (merging and breakup) as opposed to the traditional Front-Tracking approach (Shin et al., 2011). The corner points of the triangular elements, which are called marker points, are advected using a 4th-order Runge-Kutta scheme using an interpolated velocity field, obtained using cubic spline interpolation. The individual advection of the marker points will result in unevenly distributed and sized markers, which will decrease the mesh quality, and thus the accuracy of any calculations based on it over time. Therefore, the markers must be redistributed using a remeshing procedure.

In the remeshing procedure, the triangles (markers) are cut on the edges and vertices of the faces of an introduced remeshing grid, which has a grid spacing of half the size of the Eulerian grid in this work. To allow for topological changes, i.e. break-up and coalescence, the tetra-marching procedure of Yoon and Shin (2010) is implemented. After remeshing the points, the smoothing operation of Kuprat et al. is performed to correct small distortions, originating from remeshing or advection (Kuprat et al., 2001).

Table 2
Simulation settings flow around sphere, compared to empirical correlation (Schiller and Naumann, 1935).

Parameter	Value	Unit
Diameter (D_p)	1	mm
Resolution	20	$D_p/\Delta X$
L,H,D	12 D_p x 8D_p x 8D_p	mm
Position	$\frac{2}{9}$L, $\frac{1}{2}$H, $\frac{1}{2}$D	mm
Viscosity	10^{-3}	Pa s
Density	100	kg/m^3

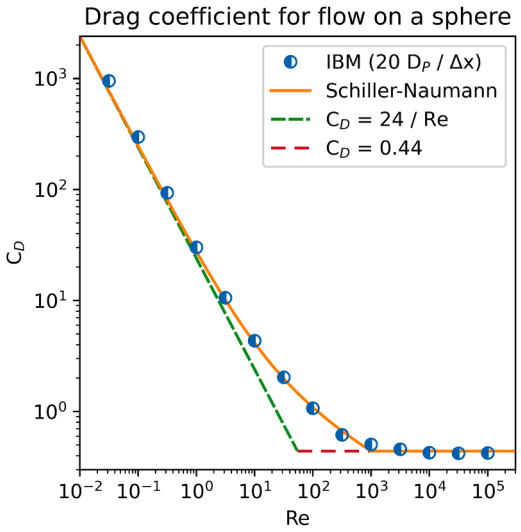

Fig. 3. Drag force coefficient for different Reynolds numbers, compared to correlation (Schiller and Naumann, 1935).

The surface tension force $\boldsymbol{F}_\sigma$ is calculated using the hybrid method of Shin et al. (2005) in Eq. (8).

$$\boldsymbol{F}_\sigma = \sigma \kappa_H \nabla \phi, \tag{8}$$

Where ϕ is the phase fraction field, σ is the surface tension coefficient, and κ_H represents the twice mean interface curvature. For further reference, the reader is referred to Rajkotwala et al. (2018). The color function ϕ is calculated by integrating the area under the triangular mesh, derived from the work of Dijkhuizen et al. (2010).

The particles considered in the work of Bunke et al. (2024) are superhydrophilic, i.e. the apparent contact angle is smaller than 15°. To correctly take this superhydrophilicity into account, a contact angle model can be applied that imposes the contact angle of 15° at the three-phase contact line. However, this results in rapid changes in the interface mesh in the initial state of lubrication of the dry particle, resulting in unphysical configurations. Therefore, we have chosen to initialize a Front-Tracking object with the same radius and position as the dry particle, i.e. the dry particle has a virtual liquid layer with a thickness of zero. As the particle is now prewetted, the superhydrophilic condition can be easily applied, and contact angles of approximately 0 can be simulated.

2.2. Fluid-solid interface

The fluid-solid interface is represented using a second-order ghost cell Immersed Boundary Method. In this method, the no-slip boundary condition is directly incorporated at the level of the discretized Navier-Stokes equations, which are solved on a structured Cartesian mesh. A detailed explanation can be found in the work of Deen et al. (2012). The applied boundary condition for the velocity on the surface of the particle is derived in Eq. (9).

$$\boldsymbol{u}_{f-s} = \boldsymbol{v}_p + \boldsymbol{\omega}_p \times (\boldsymbol{r}_s - \boldsymbol{r}_p) \tag{9}$$

Table 3
Simulation settings falling particle.

Parameter	Re = 1.5	Re = 4.1	Re = 11.6	Re = 32.2	Unit
Diameter (D_p)	1.5				cm
Resolution ($D_p/\Delta x$)	30				[−]
L,H,D	16.0 × 16.0 × 16.0				cm
initial particle position	[L/2, H/2, 8.5 * D_p]				cm
Time step	3.4×10^{-4}	2.1×10^{-4}	1.4×10^{-4}	6.7×10^{-5}	s
g	[0, 0, −9.81]				m/s^2
ρ_s	1120				kg/m^3
μ	373	212	113	58	mPa s
ρ_l	970	965	962	960	kg/m^3

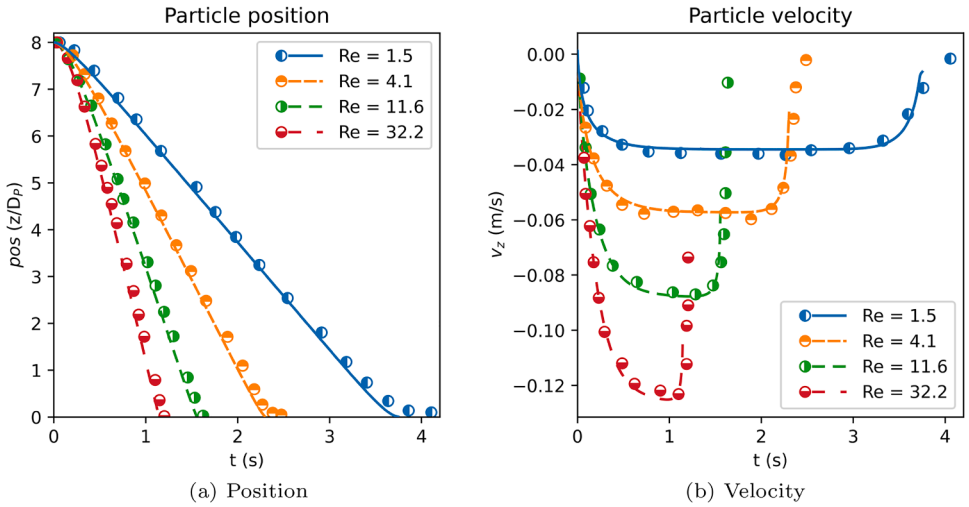

(a) Position (b) Velocity

Fig. 4. Simulation of particle position and velocity for settling particle (lines) compared to experiments from literature (markers) (ten Cate et al., 2002).

Where $\boldsymbol{u}_{f-s}$ is the Dirichlet boundary condition, $\boldsymbol{v}_p$ and $\boldsymbol{\omega}_p$ are the particle translational and angular velocity, and r_s and r_p are the position of the surface and the center of mass of the particle, respectively. These velocities are updated by solving Newton's equations of motion given by Eqs. (10) and (11).

$$m_p \frac{d\boldsymbol{v}_p}{dt} = -\oint_{\Gamma_m} (\boldsymbol{\tau}\cdot\boldsymbol{n} + p\boldsymbol{n}) dS + m_p \boldsymbol{g} \tag{10}$$

$$I_p \frac{d\boldsymbol{\omega}_p}{dt} = -\oint_{\Gamma_m} (\boldsymbol{r}_{\Gamma_m} - \boldsymbol{r}_p) \times (\boldsymbol{\tau}\cdot\boldsymbol{n}) dS \tag{11}$$

The viscous ($\boldsymbol{\tau}\cdot\boldsymbol{n}$) drag is obtained at the surface of the particle in each cell. The required projected area is taken as the area of the cell face corrected with the normals of the interface and the cell face. The form drag ($p\boldsymbol{n}$) is calculated by linear extrapolation of the pressure at the fluid notes near the object to the object surface. For a detailed explanation of these calculations, the interested reader is refered to Deen et al. (2012). m_p and I_p are the mass and inertia of the object, while $\boldsymbol{g}$ is the gravitational acceleration.

2.3. Collision model

To simulate the collision of the solid objects, the hard-sphere model of Hoomans et al. (1996) is used. The following model describes the collision dynamics (Bunke et al., 2024; Walton, 1993). For further reference the reader is referred to Walton (1993). The translational($\boldsymbol{v}_i$) and rotational velocity($\boldsymbol{\omega}_i$) are changed to $\boldsymbol{v}_i'$ and $\boldsymbol{\omega}_i'$ due to the collision as shown in Eqs. (12) and (13):

$$\boldsymbol{v}_i' = \boldsymbol{v}_i \pm \frac{\boldsymbol{J}}{m_i} \tag{12}$$

$$\boldsymbol{\omega}_i' = \boldsymbol{\omega}_i - \frac{R_i}{I_i}(\boldsymbol{n}\times\boldsymbol{J}) \tag{13}$$

where i indicates particle 1 or 2 and R_i is the radius of particle i. $\boldsymbol{n}$ is the normal to the collision plane. The slip velocity (q) is calculated with the following expression:

$$\boldsymbol{q} = \boldsymbol{v_1} - \boldsymbol{v_2} - (R_1\boldsymbol{\omega_1} + R_2\boldsymbol{\omega_2}) \times \boldsymbol{n} \tag{14}$$

From the collision, a normal restitution coefficient (e), tangential restitution coefficient (β), and an effective friction coefficient (μ) are defined as follows, using $\boldsymbol{q}$ and $\boldsymbol{q'}$ as the slip velocity before and after the collision. In the hard-sphere model these coefficients are used as model parameters (Walton, 1993) $_0$, β_0, and μ_0, respectively. Further $\boldsymbol{J}$ is the exchanged momentum during the encounter.

$$\boldsymbol{n}\cdot\boldsymbol{q'} = -e(\boldsymbol{n}\cdot\boldsymbol{q}) \tag{15}$$

$$|\boldsymbol{n}\times\boldsymbol{J}| = -\mu(\boldsymbol{n}\cdot\boldsymbol{J}) \tag{16}$$

$$\boldsymbol{n}\times\boldsymbol{q'} = -\beta(\boldsymbol{n}\times\boldsymbol{q}) \tag{17}$$

The collision angle γ is the angle between the slip velocity and the normal vector of the collision plane. The critical angle γ_0 determines the angle from which the collision mode changes from rolling to sliding. If $\gamma > \gamma_0$, a rolling collision occurs.

$$\gamma = arccot\left(\frac{\boldsymbol{q}\cdot\boldsymbol{n}}{|\boldsymbol{q}\times\boldsymbol{n}|}\right) \tag{18}$$

$$\gamma_0 = arccot\left(-\frac{2}{7}\frac{1+\beta_0}{(1+e_0)\mu_0}\right) \tag{19}$$

Further, two dimensionless metrics Ψ_1 and Ψ_2 are developed for comparison purposes, describing the normalized entrance and exit angles, which are often used in experimental studies and clearly indicate the transition from the sliding to the rolling regime.

$$\Psi_1 = -\frac{\boldsymbol{q}\cdot\boldsymbol{t}}{\boldsymbol{q}\cdot\boldsymbol{n}} = \frac{|v_t|}{|v_n|} \tag{20}$$

$$\Psi_2 = -\frac{\boldsymbol{q'}\cdot\boldsymbol{t}}{\boldsymbol{q}\cdot\boldsymbol{n}} = sign(\boldsymbol{q'}\cdot\boldsymbol{t})tan(\gamma')e_0 \tag{21}$$

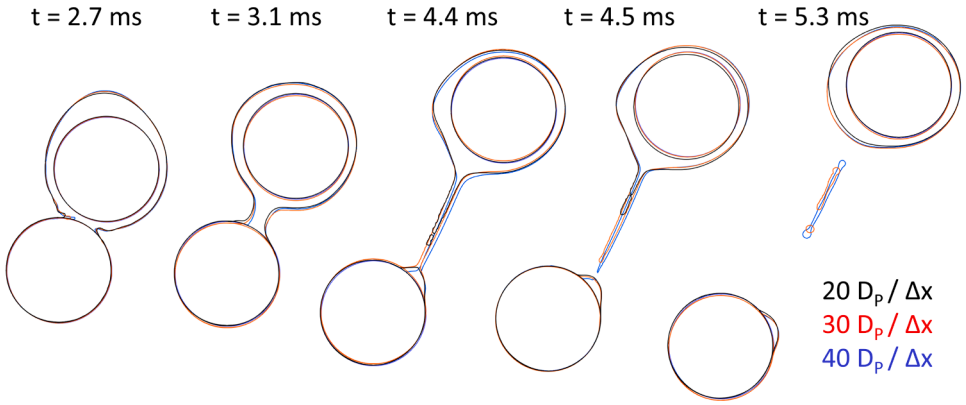

Fig. 5. Collision of a wet and a dry particle ($\gamma = 160°$) for different grid resolutions.

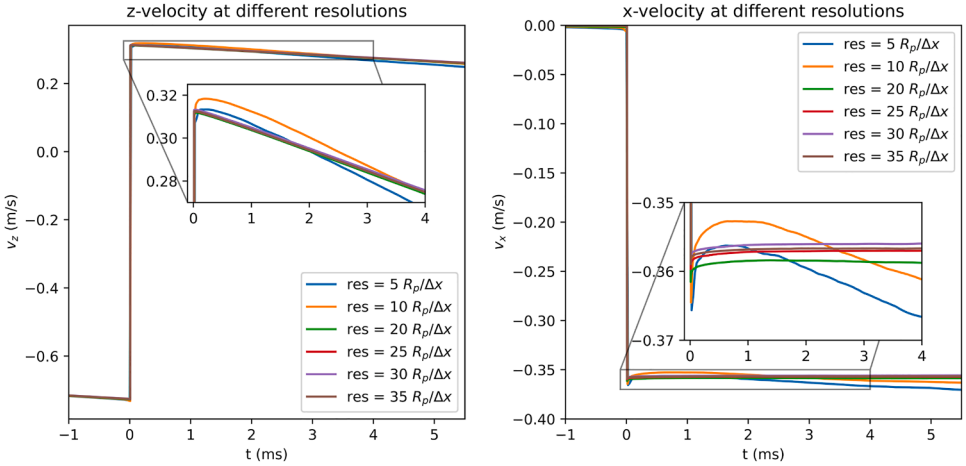

(a) velocity in collision direction (b) velocity in offset direction

Fig. 6. Particle velocity of the wet particle colliding at $\gamma = 160°$ with a dry particle for different grid resolutions.

Ψ_2 depends on the model parameters with the following relation:

$$\Psi_2 = \begin{cases} -\beta_0 \Psi_1, & \text{rolling, if } \gamma > \gamma_0. \\ \Psi_1 - \frac{7}{2}(1+e_0)\mu_0, & \text{sliding, if } \gamma \leq \gamma_0. \end{cases} \tag{22}$$

From the slip velocity and the velocities after the collisions, the values for e, β, and μ can be derived from Eqs. (15) to (17). The combination of Eqs. (20) and (22) gives the following expression for β:

$$\beta = \begin{cases} \beta_0, & \text{rolling, if } \gamma > \gamma_0. \\ \frac{7}{2}\frac{(1+e_0)\mu_0}{2|tan(\gamma)|}, & \text{sliding, if } \gamma \leq \gamma_0. \end{cases} \tag{23}$$

A similar relation is known for the friction coefficient μ:

$$\mu = \begin{cases} \mu_0\left(\frac{tan(\gamma)}{tan(\gamma_0)}\right), & \text{rolling, if } \gamma > \gamma_0. \\ \mu_0, & \text{sliding, if } \gamma \leq \gamma_0. \end{cases} \tag{24}$$

These expressions can be used to characterize the collisions. The post-processing of the simulations will be done similarly to the experimental results from the literature (Bunke et al., 2024). $\boldsymbol{q}$ is taken by determining the moment just before the liquid film lubricates the dry particle, which can be tracked with the number of Front-Tracking interfaces present in the simulation. Experimentally, this moment is visually selected. The positions and velocities are then extrapolated to the moment of solid contact. For the retrieval of $\boldsymbol{q'}$ the moment is selected when the liquid bridge is broken. Experimentally, this frame, when the liquid bridge is broken, was selected visually. The velocities and positions at that moment are extrapolated back to the moment of solid contact. In the simulations, the moment of liquid bridge rupture is determined when the number of interfaces changes from one to two.

3. Verification

The implementation of the fluid-fluid method has already been carried out and verified in earlier work (Huijgen et al., 2024a,b). Therefore the focus of the verifications in this work is on the fluid-solid interactions. In addition, the collision of particles has been verified by simulating the collision of particles with a wall and other particles and comparing it to the predictions obtained from the hard-sphere model.

To determine the correct implementation of the drag force, the drag acting on a stationary sphere in the Stokes regime (Re $\leq$ 0.1) will be examined. In this case, the drag force, the pressure field, and the velocity field can be derived analytically. In spherical coordinates, these expressions are given by Bird et al. (2007):

$$v_r = v_\infty \left[1 - \frac{3}{2}\frac{D_p}{2r} + \frac{1}{2}\left(\frac{D_p}{2r}\right)^3\right] \cos(\theta) \tag{25}$$

$$v_\phi = 0 \tag{26}$$

$$v_\theta = v_\infty \left[-1 + \frac{3}{4}\frac{D_p}{2r} + \frac{1}{4}\left(\frac{D_p}{2r}\right)^3\right] \sin(\theta) \tag{27}$$

$$p = \frac{3}{2}\frac{2\mu v_\infty}{D_p}\left(\frac{D_p}{2r}\right)^2 \cos(\theta) \tag{28}$$

$$\boldsymbol{F_{d,z}} = 3\pi\mu D_p v_\infty \tag{29}$$

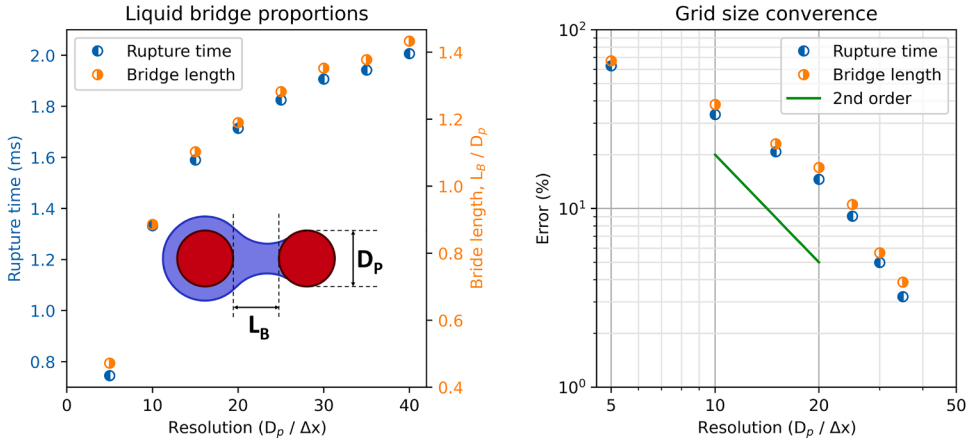

(a) liquid bridge proportions (b) Grid size dependency

Fig. 7. Grid size dependency based on liquid bridge rupture time (the time the bridge takes from forming untill rupturing) and the bridge size (the maximum length the bridge reaches before rupturing).

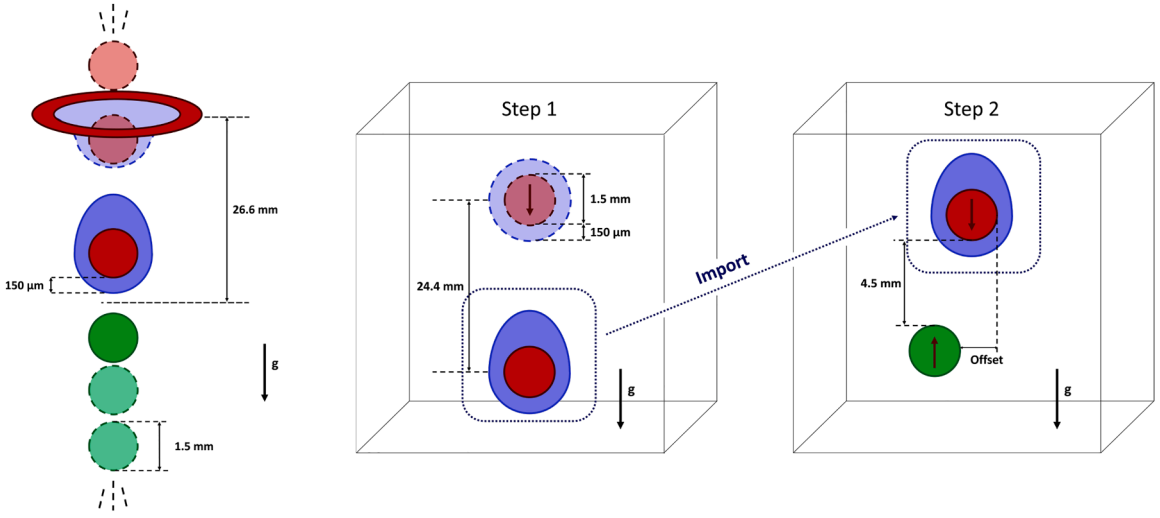

(a) Experimental setup (b) Simulation setup

Fig. 8. Schematic representation of the experimental setup used in Bunke et al. (2024) and the simulation setup.

To verify the drag force calculation, the velocity field is imposed with $\boldsymbol{v}_\infty = 10^{-4}$ and the physical properties as unity.

In Fig. 1, it can be seen that the drag force is accurately calculated. In addition, it shows that the order of convergence for the drag force calculation is second order. This is due to the second-order interpolation used in the calculation in the viscous drag component. The results overlap with those of Baltussen (2015), who used the same method. It is important to note that there are significant fluctuations in the error due to unfortunate cancellation of terms related to the exact alignment of the interface with the pressure or velocity grid.

For flow around a rotating sphere at low Reynolds numbers, there is a similar analytical solution (Bird et al., 2007). In spherical coordinates, the torque and velocity components are the following:

$$V_\phi = \omega \frac{D_p}{2} \left(\frac{D_p}{2r} \right)^2 \sin(\theta) \tag{30}$$

$$T_{d,z} = \pi \mu \omega D_p^3 \tag{31}$$

For $\omega = 10^{-5}$, the Stokes flow conditions are met. Fig. 2 shows a trend similar to Fig. 1 for the error. Again, a rate of convergence of two is found. In addition, a similar spread in the errors is found as a result of an unfortunate cancellation based on the alignment of the interface with the cells of the velocity grid.

Table 4
Simulation settings wet particle collision.

Parameter	Value	Unit
Diameter (D_p)	1.5	mm
Resolution ($D_p/\Delta x$)	30	[−]
L,H,D	$6D_p$, $6D_p$, $6D_p$	[−]
initial position particle 1	[$2.5D_p$, $3D_p$, $4.5D_p$]	[−]
initial position particle 2	[$2.5D_p$ - $3.5D_p$, $3D_p$, $1.5D_p$]	[−]
particle velocities	−0.7, 0.5	m/s
layer thickness (δ)	150	µm
viscosity (μ)	18.9	mPa.s
air density (ρ_g)	1.1845	kg/m^3
liquid density (ρ_l)	945	kg/m^3
solid density (ρ_s)	6000	kg/m^3
normal restitution coefficient (e_0)	0.998	[−]
tangential restitution coefficient (β_0)	0.406	[−]
surface tension (σ)	20.6	mN/m

4. Validation

With the drag force and torque calculation verified, the fluid-solid coupling via the Immersed Boundary Method is validated. Therefore, this validation focuses on the drag on a sphere for higher Reynolds numbers.

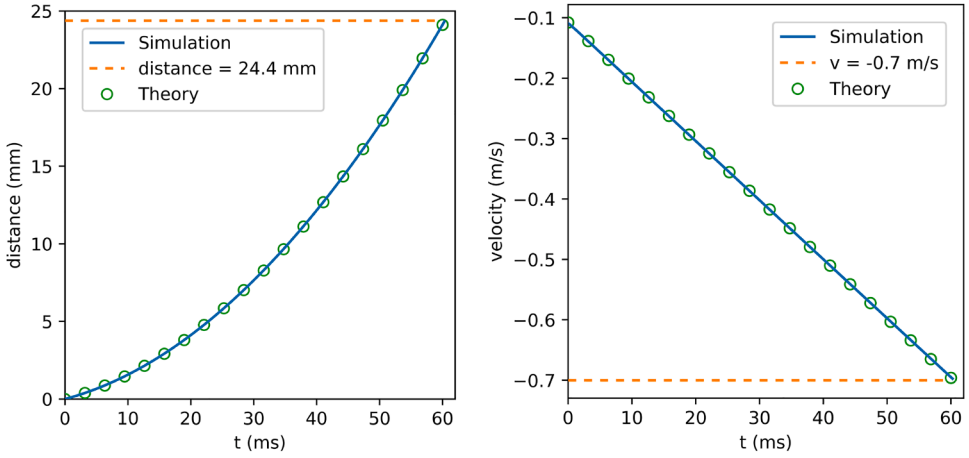

(a) Traveled distance (b) Particle velocity

Fig. 9. Particle position and velocity while settling compared to Eqs. (35) and (36).

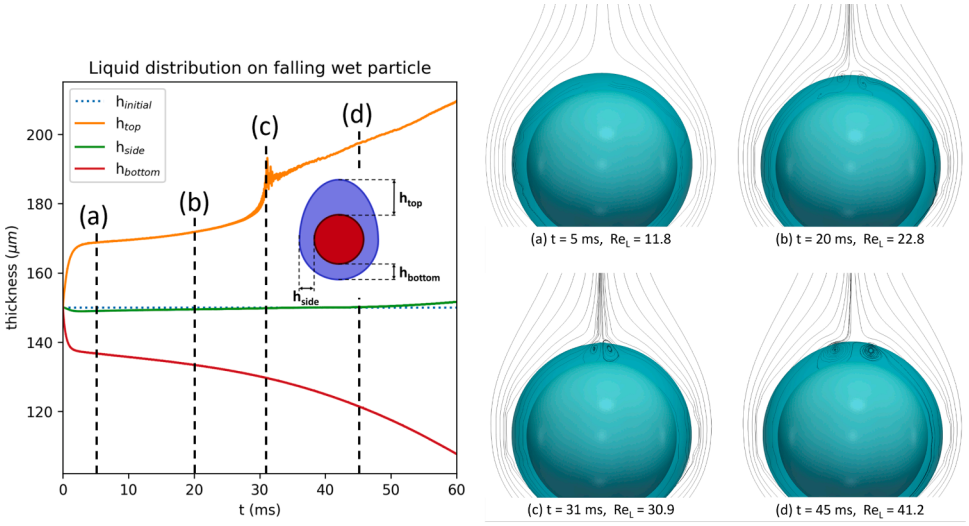

(a) Liquid layer thickness development (b) Velocity field around particle

Fig. 10. Development of the liquid layer distribution on a wet particle, with $Re_L = \frac{\rho_l u D_p}{\mu_l}$.

In this work, the correlation of Schiller-Naumann (Schiller and Naumann, 1935), as given in Eq. (32), is used for the comparison. For Stokes flow conditions, the equation will follow Eq. (29), which is rewritten as $C_D = 24 / \mathrm{Re}$.

$$C_D = \begin{cases} \frac{24}{Re}(1 + 0.15Re^{0.687}), & \text{if } Re \leq 1000 \\ 0.44, & \text{if } Re > 1000 \end{cases} \tag{32}$$

For Reynolds numbers between 10^5 and 10^6 the laminar boundary layer around the sphere will transition to turbulent boundary layers. To resolve these small Kolmogorov microscales, a much higher grid resolution is required. For the application of fluidized beds, typically Reynolds numbers up to 10^4 are encountered. Therefore, the highest Reynolds number in this simulation is 10^5. In Table 2, the simulation settings are shown. As can be observed in Fig. 3, the drag coefficient is similar to the correlation over the entire range of Reynolds numbers. On the basis of these results, it can be concluded that the no-slip boundary conditions are correctly applied to the fluid and that the fluid-solid coupling is correctly implemented. The values obtained are similar to the values obtained by Das et al. (2016), using the same Immersed Boundary Method.

In addition, the settling of a particle in a viscous liquid is simulated. These simulations are compared with the work of Ten ten Cate et al. (2002). In Table 3 the simulation settings are shown. From the results in Fig. 4, it can be concluded that the current implementation is capable of accurately simulating the sedimentation of a particle in a viscous liquid. At the end of the simulation, the particle will be close to the wall, giving an increased drag force. This force will increase once the distance is smaller. In the current model, the associated wall lubrication force is not resolved if the particle is within Δx from the wall. Therefore, there is a deviation in the position and velocity once the particle is very close to the wall. In the current work, lubrication forces are neglected.

5. Grid dependency study

To determine the grid resolution at which the solution is grid independent, a grid convergence study is performed on the collision of a dry and a wet particle with a collision angle (γ) of 160°. The simulation conditions from Table 4 are used, except for the grid resolution. Fig. 5 shows a comparison of the simulation outcome for different grid resolution. It can be observed that the formation of a liquid bridge, the moving of the contact line, and the liquid transferred into the liquid bridge are more

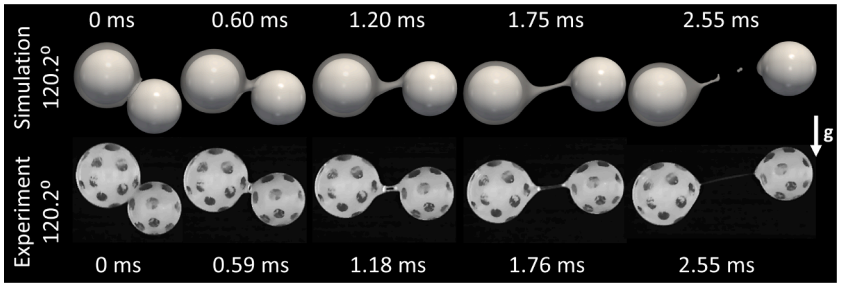

Fig. 11. Simulation of a wet particle collision using μ_{wet} with collision angle ≈ 120° compared to experiments from literature (Bunke et al., 2024).

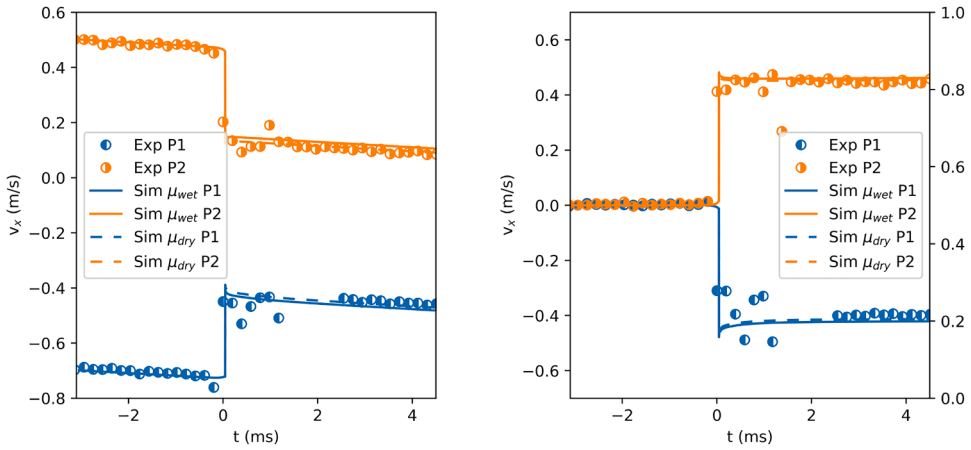

Fig. 12. Velocity development for wet particle collision with collision angle ≈ 120° using μ_{wet} (solid line) and μ_{dry} (dashed line), compared to experiments from literature (markers) (Bunke et al., 2024).

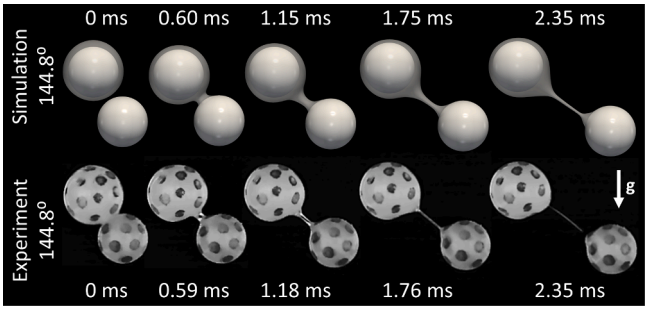

Fig. 13. Simulation of a wet particle collision using μ_{wet} with collision angle ≈ 145°, compared to experiments from literature (Bunke et al., 2024).

pronounced at lower grid resolutions. In addition, the liquid bridge rupture is delayed at lower grid resolutions. Both are related to the criteria for merging and breaking of interfaces, which occurs if interfaces are a grid cell apart from each other.

To obtain a more quantitative analysis regarding the required grid resolution, the velocity evolution of the top particle is tracked. If the grid resolution is not sufficient, both the drag force calculation and the interface reconstruction are inaccurate, yielding different values for the energy dissipation and the resulting kinetic energy and velocity. In Fig. 6, it can be seen that, except for grid resolutions 5 and 10 $D_p/\Delta x$, all other simulations converge to the same results. Although this indicates that a grid resolution of 20 $D_p/\Delta x$ would suffice to model the bulk conditions, the comparison of the interfaces in Fig. 5 indicates differently.

Another, more stringent, metric is the length of the liquid bridge. It is inherent to the numerical method that during the bridge expansion, its thickness will decrease and the liquid bridge will break if the bridge thickness is close to the grid size. Similarly to Figs. 5, 7 shows that if the grid resolution is increased, the break-up will be delayed. The duration of the collision is taken as the period when there is only one interface, i.e. the liquid bridge. The length of the bridge is taken as the difference in the distance between the particles between the formation and the rupture of the liquid bridge. It can be seen that after grid resolution 15 $D_p/\Delta x$ the order of convergence will be second-order. This second-order nature originates from the second-order discretization schemes used for the Navier-Stokes equations. As this trend continues, no minimum will be found. A grid resolution of 30 $D_p/\Delta x$ is chosen for the rest of this study, based on the shape of the complex in Fig. 5.

6. Results

Following the verification and validation of the method, we will proceed with the simulation of the experiments of Bunke et al. (2024). In these experiments, a wet particle falls and collides with a dry particle. The particles are ZrO_2 and have known binary collision parameters. The collision of two dry particles can be summarized as elastic, and the restitution coefficients are taken from the dry collision model. This choice is not so evident for the friction coefficient, as this is a material property describing the friction between the two zirconium surfaces, which is influenced by the liquid between the spheres, as it will act as a lubrication agent. In effect, the friction coefficient was determined to be 0.109 and 0.077 for the dry and wet collisions, respectively. In this work, both friction coefficients are used.

To arrange a collision between a wet and a dry particle, the falling particle will fall through a ring with a thin liquid film, effectively resulting in a liquid layer around the particle, as shown schematically in Fig. 8a. The liquid used for this is a viscous oil with a high constant viscosity, which can be assumed to behave as a Newtonian fluid.

As the distance between the collision point and the wetting ring is too large to simulate both the full path of the wetted particle falling and

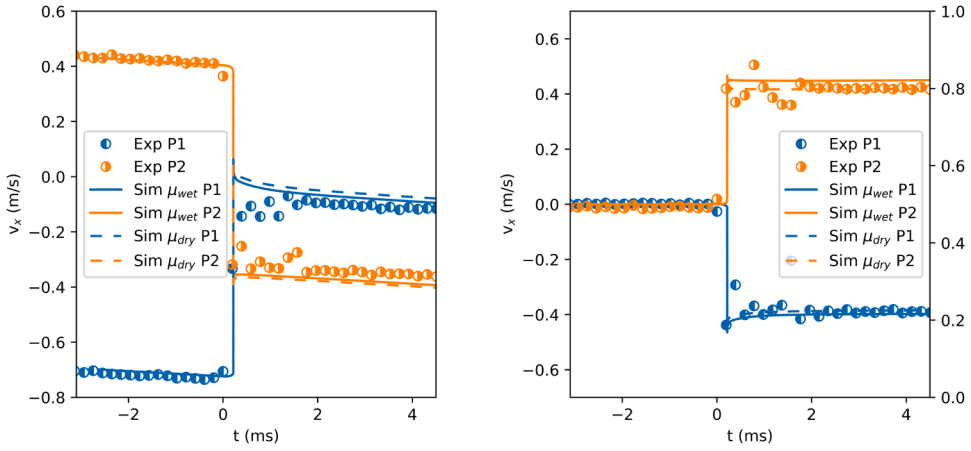

Fig. 14. Velocity development for wet particle collision with collision angle ≈ 145° using μ_{wet} (solid line) and μ_{dry} (dashed line), compared to experiments from literature (markers) (Bunke et al., 2024).

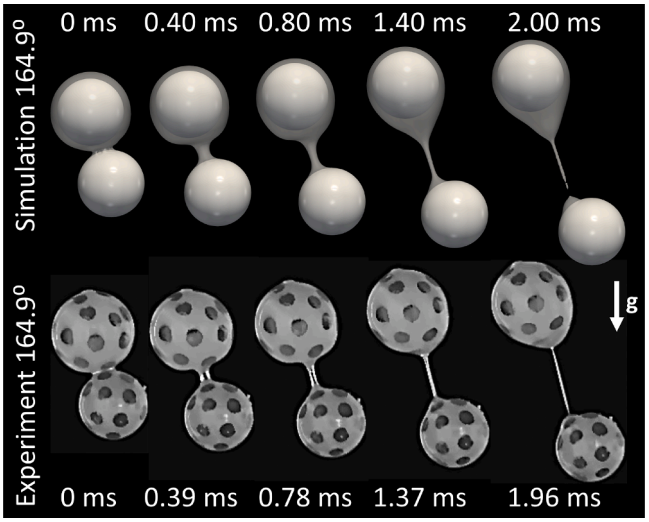

Fig. 15. Simulation of a wet particle collision using μ_{wet} with collision angle ≈ 165°, compared to experiments from literature (Bunke et al., 2024).

the subsequent collision at once, the simulation is split into two phases. I.e. the decent of the wet particle and its collision with the dry particle. In addition, there is an added benefit that the velocity profile around the descending wet particle will also develop, yielding more realistic replication of the experimental collision scenario.

For the descent of the wetted particle, an initial velocity of the particle and a stationary surrounding droplet are initialized. The simulation is continued until the particle reaches the field of view. The shape and position of the particle and droplet are then being copied to the second phase of the simulation. A dry particle is added that rises from the bottom of the field of view in step 2. These two steps are covered in the following two sections. In Table 4, the simulation properties are shown. The maximum capillary number in the simulation ($Ca = \frac{\mu u}{\sigma}$) is 1.3, which means that both the viscous forces and the capillary forces are important during the encounter.

6.1. Liquid distribution

First, the simulation results for the wet falling particle are discussed. To determine the correct initial velocity of the particle, a force balance is solved for the falling particle. From the experiments, the particle has a velocity of 0.7 ± 0.003 m/s when entering the field of view. In addition, the distance traveled by the particle can be determined from the experimental set-up (26.6 − 1.5 D_p = 24.4 mm). Using the Schiller-Naumann correlation (Schiller and Naumann, 1935), the drag force and the gravitational force can be calculated.

$$F_g = \frac{4}{3}\left(\frac{D_p}{2}\right)^3 \pi \rho_s g \approx -2 \times 10^{-5}\ N \tag{33}$$

$$F_d = \frac{1}{2}\rho_g v^2 C_d \pi D_p \approx 8 \times 10^{-7}\ N \tag{34}$$

As the gravity force is significantly larger than the drag force, the particle motion during settling can be described using the general equations of linear motion using g as the acceleration:

$$s(t) = s_0 + v_0 t + \frac{1}{2} g t^2 \tag{35}$$

$$v(t) = v_0 + g t \tag{36}$$

Based on these equations, the initial velocity of the particle can be determined for the known final velocity (v) and distance ($x - x_0$).

$$v_0 = \sqrt{v^2 - 2\ g(x - x_0)} \approx 0.11\ m/s \tag{37}$$

The simulations of the settling of the wet particle are started using this initial velocity and the conditions specified in Table 4. To maintain a suitable domain to cover the flow field around the particle and especially the wake behind the particle, the window shifting concept is applied to ensure that the particle stays at the initial position (Deen et al., 2012). The position and velocity of the falling wetted particle are shown in Fig. 9, where the theoretical extimate results from Eqs. (35) and (36). It is apparent that the assumption of neglecting the drag force is valid, as the velocity and position of the particle are predicted by Eqs. (35) and (36). During the later stages the velocity starts to deviate due to the increased drag force at higher Reynolds numbers.

During the fall of the particle, the liquid is redistributed over the surface of the particle, while the velocity field develops around the particle. Fig. 10a illustrates the development of the liquid layer. Initially, the liquid layer rapidly deforms as a result of the sudden movement of the particle. At point *a* in Fig. 10b, the flow profile shows unseparated flow, resulting in linear increase in liquid layer thickness. When the velocity of the particle increases, the onset of separation is reached (point *b* in Fig. 10b), which occurs at approximately $Re = 20$ as expected (Clift et al., 1978). The reversal of the vorticity, which begins at this onset of separation, causes a rapid increase in the liquid layer thickness. After point *c* in Fig. 10b, the flow profile transitions to a steady wake region, which shows a steady increase of the liquid layer due to the stable slowly growing wake (Clift et al., 1978). Comparing point *c* and *d* in Fig. 10b, it can be concluded that the increase in wake volume causes an increase in the thickness of the liquid layer at the rear part of the particle. At t = 60 ms, the final shape of the complex is established, which will be used for collisions with dry particles, as discussed in the next section.

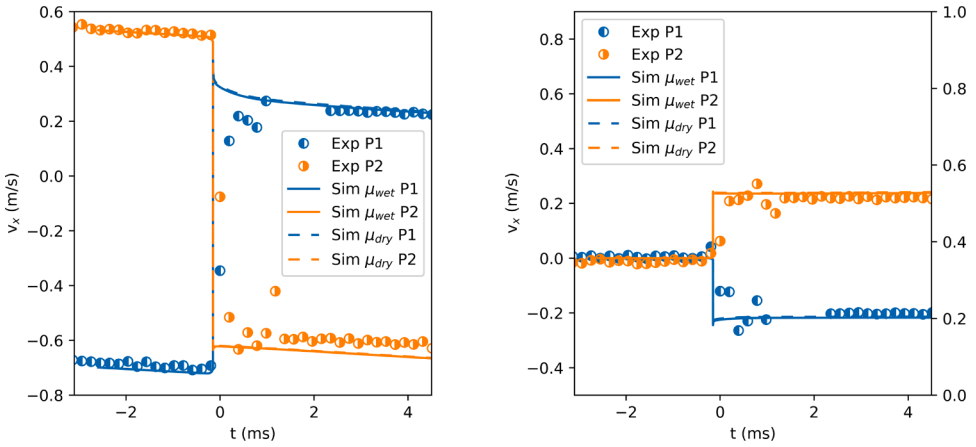

Fig. 16. Velocity development for wet particle collision with collision angle ≈ 165° using μ_{wet} (solid line) and μ_{dry} (dashed line), compared to experiments from literature (markers) (Bunke et al., 2024).

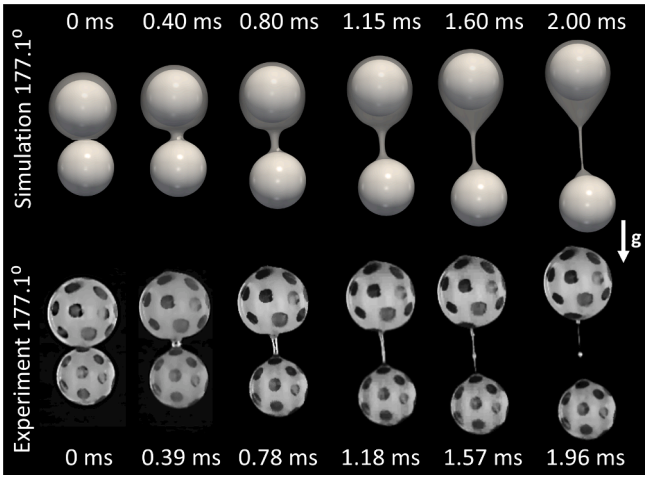

Fig. 17. Simulation of a wet particle collision using μ_{wet} with collision angle ≈ 180°, compared to experiments from literature (Bunke et al., 2024).

Table 5
Different simulation cases.

case	Collision angle [°]	velocity wet particle [m/s]	velocity dry particle [m/s]
1	120.2	0.7	0.50
2	144.8	0.7	0.43
3	164.9	0.7	0.53
4	177.1	0.7	0.51

6.2. Comparison with experiments

For the collisions, the simulation results of the falling wet particle are imported to a new simulation domain, while a second particle is added. The 4 cases studied in this work are given in Table 5 and the results are compared with the experimental data of Bunke et al. (2024). As the velocity of the dry particle fluctuates significantly, the experimentally observed value is used.

In case 1 an oblique collision is studied. Fig. 11 shows the comparison of the simulation with the experiments. The visualization of the simulations are similar for both μ_{wet} and μ_{dry}. Therefore, Fig. 11 shows only the results using μ_{wet}. In addition, the simulated interface topology and arrangement of the particles are similar to the experiments. It is difficult to compare the break-up of the liquid bridge as numerically the break-up is influenced to some extent by the chosen grid size. Besides, the experimental visualization of a very thin bridge is challenging and therefore it is not trivial to deduce if the bridge is broken.

When the evolution of the simulated particle velocities is compared with the experiments (See Fig. 12) good agreement is obtained. In this comparison, it should be noted that the experimental data between 0 and 2.5 ms is not reliable as it is based on the particle detection of the particles from the images, which is less accurate when the liquid bridge is present. Based on the simulation results using μ_{wet} and μ_{dry} in Fig. 12 it is not possible to conclude which of the friction coefficient should be used.

For the less oblique collision in Case 2, a similar result is observed, as shown in Figs. 13 and 14. This includes similar results when using μ_{wet} and μ_{dry} for the friction coefficient. In this case, the experimental difficulty to capture the break-up of the liquid bridge is nicely captured at $t = 2.35$ ms. The development of the interface topology and the particle positions is almost identical, except for the break-up of the liquid bridge. This indicates that we can use these simulations to gain information on the dynamics that occur in these collisions, which is not possible using experiments.

When examining the amount of liquid in the liquid bridge, there seems to be more liquid in the liquid bridge in the simulations compared to the experiment, while the liquid layer thickness on the wet particles is the same as in the experiments. As can be seen in Figs. 15 and 17, the volume of the bridge (t = 0.40 ms) and the amount of liquid that remains on the initially wet particle (t = 2.00 ms) appear to be larger for the simulation. A likely explanation for this discrepancy is the non-uniform distribution of liquid on the particle. Even a slight inaccuracy in the wetting procedure (e.g. ring circularity, positioning, or roughness) could break the axisymmetry through the vertical axis, leading to uneven distribution of the liquid layer on the particle. In contrast, the simulation assumes a fully symmetric distribution along this axis. In addition, a small roughness of the particle could entrain a part of the liquid on the surface of the particle, preventing it from moving toward the liquid bridge. This roughness of the particles is not taken into account in the current modeling and might be added in future work by subgrid-scale modeling of these effects on the movement of the gas-liquid interface. It can be seen in Fig. 16 that the particle velocities are similar for both simulations and the experiments, where the difference between the wet and dry friction coefficient is smaller compared to the lower collision angles. In Fig. 18 the velocities for both friction coefficients are nearly identical, which is logical as the tangential component is negligible for near head-on collisions ensuring that there is no effect of the friction coefficient.

For prediction of the interactions of these collisions between wet and dry particles, it is interesting to identify the main source of energy dissipation during the collision, which will be determined using

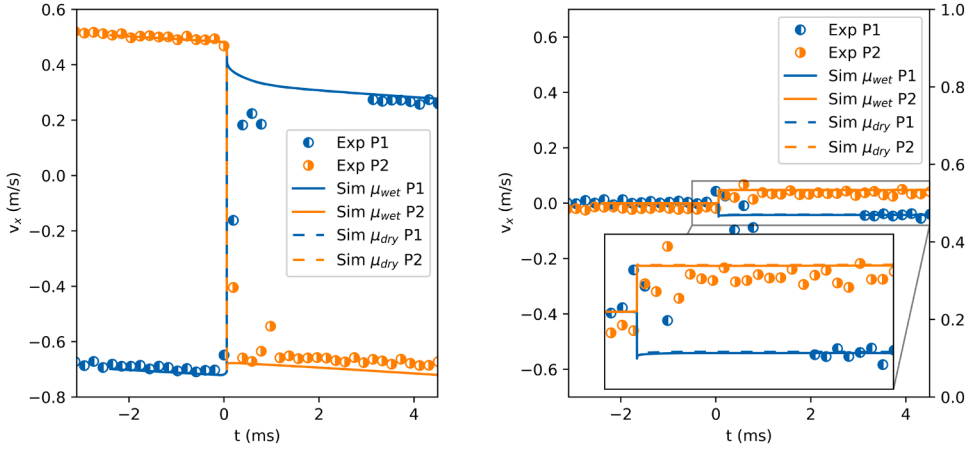

Fig. 18. Velocity development for wet particle collision with collision angle ≈ 180° using μ_{wet} (solid line) and μ_{dry} (dashed line), compared to experiments from literature (markers) (Bunke et al., 2024).

the simulated evolution of the particle velocities, as the experimental measurements of the velocities are not reliable during the extension of the bridge. Based on Figs. 12, 14, 16, and 18, it is clear that the main decrease in velocity occurs just after the collision of the particles (i.e. in the first moments of the extension of the bridge), which is most clearly shown for the initially wet particle as the liquid layer deposited on this particle initially contributes to the liquid bridge. In Fig. 19 a head-on collision is performed without gravity to remove any effects other than the effects of the collision and the formation of the liquid bridge. The flow field around the particle is visualized and shows the liquid transfer from the wet particle to the liquid bridge, especially at point b. As the liquid bridge becomes thin, this effect will be less pronounced as less liquid is transferred to the liquid bridge, shown at points c and d.

Figs. 16 and 18 show a small deviation in vertical velocity after the collision when comparing the simulation results with the experimental results. This difference arises from the lubrication force. The effect of this lubrication is clearly shown in point a in Fig. 19, which is at the moment the dry particle penetrates the liquid layer of the wet particle. At this moment, the liquid between the particles is pushed out, resulting in an increase in pressure and a so-called lubrication force. When there is no pressure node between the particles, these effects cannot be accounted for in the model and a sub-grid model is required to further improve the match between the experimental and numerical results.

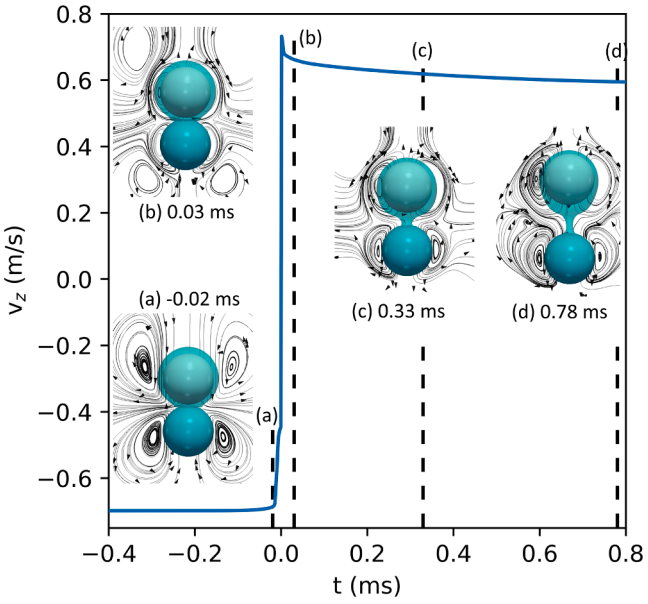

Fig. 19. Simulation of a wet particle collision using μ_{wet} with collision angle = 180° without gravity compared to z-velocity.

6.3. Restitution coefficient

In Fig. 20, the collision parameters derived from the simulations are compared to the experimentally obtained model from the literature (Bunke et al., 2024). These simulations are conducted in the absence of gravity to isolate collision dynamics and eliminating the need for z-velocity adjustments. The simulations employ the dry normal and tangential restitution coefficients from Table 4. Since Figs. 12, 14, 16, and 18 did not clearly indicate which friction coefficient to apply, the dry and wet friction coefficients are considered in this section and are shown separately.

The simulations using the wet friction coefficient are fitted to a new collision model using the *least_square* method from Python's *SciPy* library. The collision parameters are presented in Table 6 and plotted against the data in Fig. 20. In Fig. 20a, the calculated normal restitution coefficient exceeds the experimental values; a difference is attributed to the lubrication force, as discussed in the previous section. The usage of the different friction coefficients does not show significant differences, which is expected because the friction coefficient does not influence the normal component of the collision. Although both μ_{wet} and μ_{dry} show similar trends for the tangential restitution coefficient (Fig. 20b), the value of the tangential restitution coefficient is higher when μ_{dry}, especially in the sliding regime ($\gamma < 159°$). In the sliding regime, the restitution coefficients using the wet friction coefficient and the wet experimental data exhibit close agreement, while the simulations using the dry friction coefficient align with the dry experimental model. This effect of the chosen friction coefficient is also clear in the computed friction coefficient in Fig. 20c, which clearly shows that the simulation using the wet friction coefficient closely matches the wet experimental model, and the simulation with the dry friction coefficient matches the dry experimental model. As the simulation using the wet friction coefficient show close agreement with the experimental data, it can be concluded that the friction coefficient is not affected by the development of the flow field or the liquid bridge and should be considered as a material property. To incorporate this effect in CFD, the wet friction coefficient from experiments can be used directly, or a sub-grid model can be developed to incorporate the effect of this lubrication. The comparison of Ψ_1 and Ψ_2 in Fig. 20d illustrates that the normalized evolution of the collisions follows the same trend as the experimental results using the wet friction coefficient. For both the rolling ($\Psi_1 < 0.39$) and the sliding ($\Psi_1 > 0.39$) regions, similar behavior is observed in both the simulations and the experiments. Furthermore, the transition from the sliding to the rolling

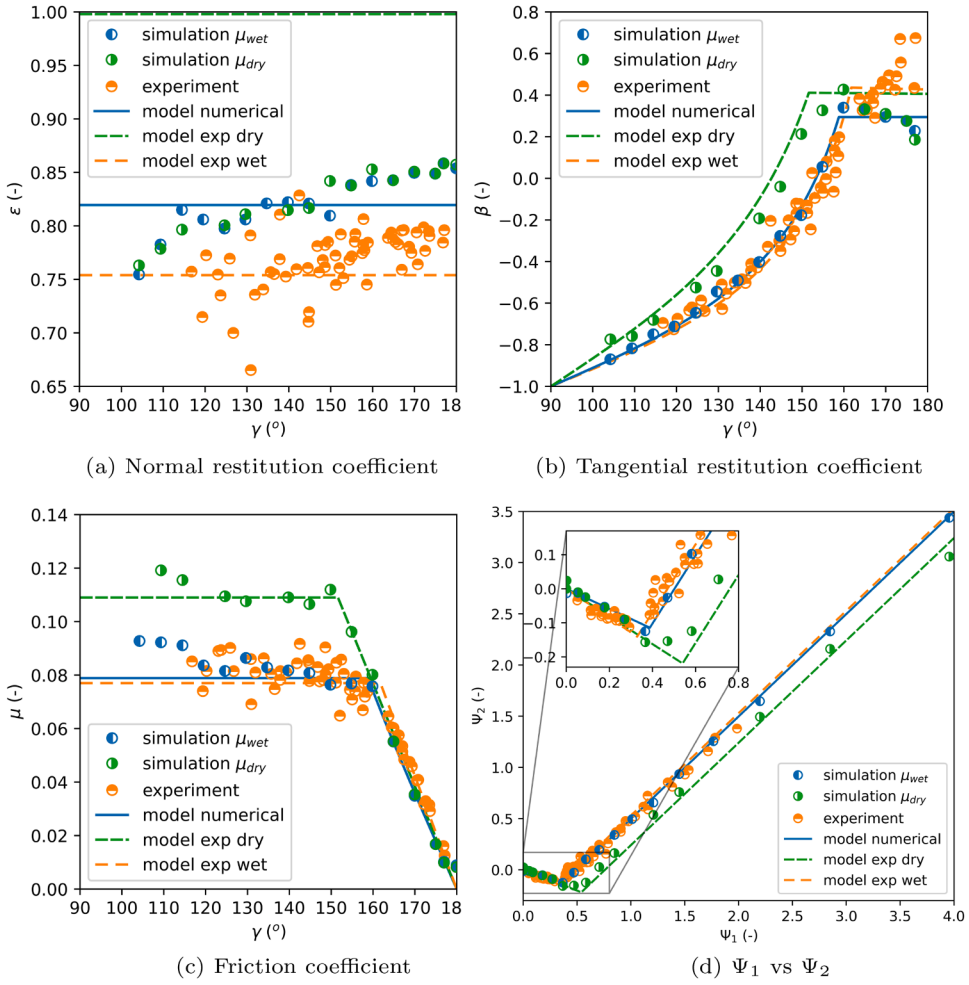

(a) Normal restitution coefficient (b) Tangential restitution coefficient

(c) Friction coefficient (d) Ψ_1 vs Ψ_2

Fig. 20. Collision parameters from simulations compared to experiments and wet and dry collision model from literature (Bunke et al., 2024).

Table 6
Comparison of model parameters and collision parameters between wet collisions in simulations and dry and wet collisions in experiments (Bunke et al., 2024).

Variable	Experiment dry (Bunke et al., 2024)	Experiment wet (Bunke et al., 2024)	Simulation wet
e_0	0.998	0.754	0.8196
β_0	0.406	0.427	0.2946
μ_0	0.109	0.077	0.07887
γ_0	151.63	161.78	158.79

region is consistent with the experimental transition, as the values for γ_0 differ by only a few percentage points.

7. Conclusion

To enhance the knowledge about agglomeration, it is important to understand the formation and rupture of a liquid bridge upon collision of two particles. Therefore, this work focuses on understanding the interaction of a wet and a dry particle. These interactions were studied with a hybrid LFRM Immersed Boundary Method (IBM). Following verification and validation of the method, the simulation results were compared with the experimental data of Bunke et al. (2024). In addition to the shape of the formed complex, the velocities of the particles before and after the collision are nearly identical. In addition, the main source of the energy dissipation identified as the extension of the liquid film just after the collision. Based on the simulation results, effective collision parameters were fitted. The results confirm that the wet friction coefficient is a material property that is unaffected by the flow field or liquid bridge dynamics and should therefore be obtained from experiments.

To improve the results, the roughness of the particle should be included, as the roughness might entrap some of the liquid. Additionally, it was inferred that sub-grid repulsion forces are at play which require the implementation of a lubrication model. In further endeavors, a parametric study should be performed to translate these results to more general applications. This could be extended to the collision of two wet particles or partially wet particles to achieve a conclusive picture of the full dynamics.

CRediT authorship contribution statement

A.H. Huijgen: Conceptualization, Data curation, Formal analysis, Investigation, Methodology, Software, Validation, Visualization, Writing – original draft; **T.J.A. Janssen:** Methodology, Software, Conceptualization, Writing – review & editing; **F. Bunke:** Validation, Writing – review & editing; **S. Pietsch-Braune:** Supervision, Validation, Writing – review & editing; **S. Heinrich:** Supervision, Validation, Writing – review & editing; **J.A.M. Kuipers:** Formal analysis, Funding acquisition, Methodology, Resources, Supervision, Writing – review & editing; **M.W. Baltussen:** Conceptualization, Formal analysis, Funding acquisition, Investigation, Methodology, Project administration, Resources, Software, Supervision, Writing – review & editing.

Data availability

The raw data of this research can be found in DOI: 10.4121/61d23b22-7cde-43a4-ba56-8015f47833c3

Declaration of competing interest

The authors declare the following financial interests/personal relationships which may be considered as potential competing interests:

A.H. Huijgen, J.A.M. Kuipers and M.W. Baltussen reports financial support was provided by Dutch Research Council. If there are other authors, they declare that they have no known competing financial interests or personal relationships that could have appeared to influence the work reported in this paper.

Acknowledgments

This publication is part of the project Understanding of wet agglomeration of non-spherical particles in fluidized beds with project number 19951 of the Open Technology Programme, which is financed by the Dutch Research Council (NWO). This work was funded by the Deutsche Forschungsgemeinschaft (DFG, German Research Foundation) – project number 438775980.

References

Antonyuk, S., Heinrich, S., Deen, N., Kuipers, J.A.M., 2009. Influence of liquid layers on energy absorption during particle impact. Particuology 7 (4), 245–259.
Baltussen, M.W., 2015. Bubbles on the cutting edge : direct numerical simulations of gas-liquid-solid three-phase flows. Ph.D. thesis. Eindhoven University of Technology department of Chemical Engineering and Chemistry.
Bird, R.B., Stewart, W.E., Lightfoot, E.N., 2007. Transport Phenomena revised second ed.. John Wiley & Sons, Ltd.
Brackbill, J.U., Kothe, D.B., Zemach, C., 1992. A continuum method for modeling surface tension. J. Comput. Phys. 100, 335354.
Bunke, F., Pietsch-Braune, S., Heinrich, S., 2024. Three-dimensional measurement method of binary particle collisions under dry and wet conditions. Chem. Eng. J. 489 (April), 151016.
Team The Trilinos Project, 2023. The Trilinos Project Website. https://trilinos.github.io.
ten Cate, A., Nieuwstad, C.H., Derksen, J.J., Van den Akker, H.E.A., 2002. Particle imaging velocimetry experiments and lattice-Botlzmann simulations on a single sphere settling under gravity. Phys. Fluids 14 (11), 4012–4025.
Centrella, J., Wilson, J.R., 1984. Planar numerical cosmology. II—The difference equations and numerical tests. Astrophys. J. Suppl. Ser. 54, 229.
Clift, R., Grace, J., Weber, M.E., 1978. Bubbles, Drops, and Particles. Academic Press Inc., New York. first ed..
Das, S., Deen, N.G., Kuipers, J.A.M., 2016. Immersed boundary method (IBM) based direct numerical simulation of open-cell solid foams: hydrodynamics. AlChE J. 63 (3), 1152–1173.
Deen, N.G., Kriebitzsch, S. H.L., van der Hoef, M.A., Kuipers, J.A.M., 2012. Direct numerical simulation of flow and heat transfer in dense fluid–particle systems. Chem. Eng. Sci. 81, 329–344.
Dijkhuizen, W., Roghair, I., Van Sint Annaland, M., Kuipers, J.A.M., 2010. DNS of gas bubbles behaviour using an improved 3D front tracking model-Model development. Chem. Eng. Sci. 65 (4), 1427–1437.
Donahue, C.M., Brewer, W.M., Davis, R.H., Hrenya, C.M., 2012. Agglomeration and deagglomeration of rotating wet doublets. J. Fluid Mech. 708, 128–148.
Donahue, C.M., Hrenya, C.M., Davis, R.H., 2010a. Stokes's Cradle: Newton's Cradle with liquid coating. Phys. Rev. Lett. 105 (3), 1–2. https://doi.org/10.1103/PhysRevLett.105.034501
Donahue, C.M., Hrenya, C.M., Davis, R.H., Nakagawa, K.J., Zelinskaya, A.P., Joseph, G.G., 2010b. Stokes' Cradle: normal three-body collisions between wetted particles. J. Fluid Mech. 650, 479–504.
Fan, Z., Liu, D., Liang, C., Chen, X., 2024. Numerical simulation of collision dynamics between a dry particle and a liquid-coated wet particle. Powder Technol. 434 (September 2023), 119308.
Hoomans, B.P.B., Kuipers, J.A.M., Briels, W.J., Van Swaaij, W.P.M., 1996. Discrete particle simulation of bubble and slug formation in a 2D gas-Fluidised bed: a hard-sphere approach. Science 51 (1), 99–118.
Huijgen, A.H., Durubal, P.M., Llamas, C.G., Buist, K.A., Kuipers, J.A.M., Baltussen, M.W., 2024a. Characterizing binary droplet collisions of power-law fluids. AlChE J. 71.
Huijgen, A.H., García Llamas, C., Durubal, P.M., Buist, K.A., Kuipers, J.A.M., Baltussen, M.W., 2024b. Numerical investigation of non-Newtonian droplet collisions: comparison of volume of fluid and the local front reconstruction method with experimental data. Chem. Eng. Sci. 299, 120428.
Jain, D., Deen, N.G., Kuipers, J.A.M., Antonyuk, S., Heinrich, S., 2012. Direct numerical simulation of particle impact on thin liquid films using a combined volume of fluid and immersed boundary method. Chem. Eng. Sci. 69 (1), 530–540.
Kan, H., Nakamura, H., Watano, S., 2015. Numerical simulation of particle-particle adhesion by dynamic liquid bridge. Chem. Eng. Sci. 138, 607–615.
Kan, H., Nakamura, H., Watano, S., 2016. Effect of particle wettability on particle-particle adhesion of colliding particles through droplet. Powder Technol. 302, 406–413.
Kan, H., Nakamura, H., Watano, S., 2018. Effect of collision angle on particle-particle adhesion of colliding particles through liquid droplet. Adv. Powder Technol. 29 (6), 1317–1322.
Kuprat, A., Khamayseh, A., George, D., Larkey, L., 2001. Volume conserving smoothing for piecewise linear curves, surfaces, and triple lines. J. Comput. Phys. 172 (1), 99–118.
Ma, J., Liu, D., Chen, X., 2016. Normal and oblique impacts between smooth spheres and liquid layers: liquid bridge and restitution coefficient. Powder Technol. 301, 747–759.
Milacic, E., Rantong, D.R., Kuipers, J.A.M., Baltussen, M.W., 2023. Temperature distribution in fluidized beds of porous particles with LiquidInjection. Chemie-Ingenieur-Technik 95 (1–2), 129–135.
Mirsandi, H., Rajkotwala, A.H., Baltussen, M.W., Peters, E.A.J.F., Kuipers, J.A.M., 2018. Numerical simulation of bubble formation with a moving contact line using local front reconstruction method. Chem. Eng. Sci. 187, 415–431.
Rajkotwala, A.H., Mirsandi, H., Peters, E.A.J.F., Baltussen, M.W., Van Der Geld, C.W.M., Kuerten, J.G.M., Kuipers, J.A.M., 2018. Extension of local front reconstruction method with controlled coalescence model. Phys. Fluids 30 (2), 022102.
Schiller, L., Naumann, A., 1935. A drag coefficient correlation. Z. Ver. Dtsch. Ing. 77, 318–320.
Shao, L., Liu, D., Ma, J., Chen, X., 2022. Normal collision between partially wetted particles by using direct numerical simulation. Chem. Eng. Sci. 247, 117090.
Shin, S., Abdel-Khalik, S.I., Daru, V., Juric, D., 2005. Accurate representation of surface tension using the level contour reconstruction method. J. Comput. Phys. 203 (2), 493–516.
Shin, S., Yoon, I., Juric, D., 2011. The local front reconstruction method for direct simulation of two- and three-dimensional multiphase flows. J. Comput. Phys. 230 (17), 6605–6646.
Tang, Y., Kuipers, J.A.M., Buck, B., Heinrich, S., Deen, N.G., 2017. Interface-resolved simulations of normal collisions of spheres on a wet surface. AlChE J. 63 (11), 4774–4787.
Van Leer, B., 1977. Towards the ultimate conservative difference scheme. IV. A new approach to numerical convection. J. Comput. Phys. 23 (3), 276–299.
Van Sint Annaland, M., Deen, N.G., Kuipers, J.A.M., 2005. Numerical simulation of gas bubbles behaviour using a three-dimensional volume of fluid method. Chem. Eng. Sci. 60 (11), 2999–3011.
van der Vorst, H.A., 1992. Bi-CGSTAB: a fast and smoothly converging variant of Bi-CG for the solution of nonsymmetric linear systems. SIAM J. Sci. Stat. Comput. 13 (2), 631–644.
Walton, O.R., 1993. Particulate Two-Phase Flow. Butterworth-Heinemann, StoneHam. particulat ed..
Yoon, I., Shin, S., 2010. Tetra-marching procedure for high order level contour reconstruction method. WIT Trans. Eng. Sci. 69, 507–518.